Analytica Chimica Acta 1173 (2021) 338678

Contents lists available at ScienceDirect

Analytica Chimica Acta

journal homepage: www.elsevier.com/locate/aca

Broadband electrical impedance as a novel characterization of oxidative stress in single L6 skeletal muscle cells

Caroline Ferguson [a, 1], Niccolo Pini [b, 1], Xiaotian Du [c], Marco Farina [d], James M.C. Hwang [c], Tiziana Pietrangelo [b], Xuanhong Cheng [a, e, *]

[a] Department of Bioengineering, Lehigh University, Bethlehem, PA, USA
[b] Department of Neuroscience, Imaging, and Clinical Science, University G. D'Annuzio, Chieti-Pescara, Italy
[c] Department of Electrical Engineering, Lehigh University, Bethlehem, PA, USA
[d] Department of Engineering of Information, University Politecnica delle Marche, Marche, Italy
[e] Department of Materials Science and Engineering, Lehigh University, Bethlehem, PA, USA

HIGHLIGHTS

- Oxidative stress (OS) related diseases like ME/CFS lack unique biophysical markers.
- Differences between stressed and regular cells can be sensed via broadband sensing.
- Electrical signatures of cells experiencing OS have wider spread at GHz frequencies.
- Electrical difference can be tied to calcium flux within the cytoplasm.

GRAPHICAL ABSTRACT

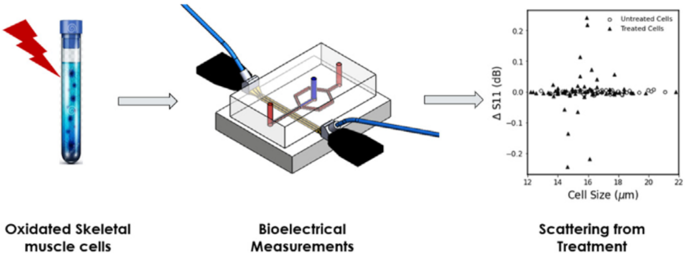

ARTICLE INFO

Article history:
Received 4 May 2021
Received in revised form
18 May 2021
Accepted 20 May 2021
Available online 25 May 2021

Keywords:
Oxidative stress
Broadband electrical sensing
Dielectric
Calcium signaling
Microfluidic
Single cell

ABSTRACT

Oxidative stress (OS) is one of the leading causes of cytotoxicity and is linked to many human physio-pathological conditions. In particular, myalgic encephalomyelitis/chronic fatigue syndrome (ME/CFS) induced by OS is debilitating to quality of life, while no clear biological markers have been identified for diagnostic measures. Recently, impedance measurements of peripheral blood cells of ME/CFS patients have been shown as a promising approach to diagnose the disease. Inspired by this study and aiming to interrogate muscle cells directly, we investigated if broadband measurements of single muscle cells could differentiate normal and oxidatively stressed cell populations. We first optimized a protocol through H_2O_2 treatment to introduce oxidative stress to cultured rat L6 skeletal muscle cells. The treated cells were further characterized through broadband impedance spectroscopy of single cells using a microfluidic lab-on-a-chip system. The resulting dielectric properties of cytoplasm permittivity and conductivity are electrically distinct from normally cultured cells. The reflection and transmission coefficients, ΔS11 and ΔS21, of the normal cells are tightly clustered and closely resemble those of the cell-free solution across the frequency range of 9 kHz to 9 GHz. On the other hand, dielectric properties of the oxidized cells have a wide distribution in the GHz range, deviating both in the positive and negative directions from the normally cultured cells. Simulation results guide our hypothesis that the dielectric differences could be linked to ion alterations, while calcium imaging directly supports the contribution of calcium flux to the observed deviation of S parameters. The unique electrical profile associated with oxidized cells in the GHz frequencies provide a framework for future development of technologies to diagnose oxidative-stress related diseases such as ME/CFS.

---

[*] Corresponding author. Department of Bioengineering, Lehigh University, Bethlehem, PA, USA.
E-mail address: xuc207@lehigh.edu (X. Cheng).

[1] Caroline Ferguson and Niccolo Pini share equal contributions to this research.

https://doi.org/10.1016/j.aca.2021.338678

1. Introduction

Chronic impairment of the cellular redox homeostasis leads to oxidative stress (OS) [1]. OS is one of the most important biochemical parameters investigated in cell biology due to its role in many physio-pathological conditions. It is one of the leading causes of toxicity due to the interactions of reactive oxygen species with a myriad of cellular macromolecules such as DNA, lipid, and proteins. Typically, OS is investigated by enzymatic, Western blot, real time-PCR and colorimetric assays, all of which are expensive, time consuming, and require trained technicians [2]. In addition, these assays are terminal approaches only performed on cell lysate or permeabilized cells, therefore not directly correlated with the functional aspects of the oxidative stress. These technical constraints demand new techniques that can correlate OS to functional alteration on living cells for both fundamental studies and clinical diagnosis.

The pathological consequences of OS are attributed to pro-oxidants changing to their thiol/disulfide redox state, which subsequently lead to mitochondrial impairment and chronic inflammation [3]. OS is involved in many physio-pathological conditions such as myalgic encephalomyelitis/chronic fatigue syndromes (ME/CFS), cancer, autoimmune diseases, metabolic syndrome and ageing [3–5]. In particular, CFS is related to OS degrading skeletal muscle function over an extended period of time [6–8]. ME/CFS is a disabling clinical condition characterized by unexplained and persistent post-exertional fatigue that drastically reduces quality of life in patients [9,10]. Diagnostic tools for this disease are required all the more in the wake of the COVID-19 pandemic, considering so many symptoms of ME/CFS are shared with lingering COVID patient symptoms [11]. The lack of a clear biological marker for ME/CFS presents a great challenge for its diagnosis [12–19], while recent research revealed that the skeletal muscles of ME/CFS patients show mitochondrial impairment and altered intracellular calcium homeostasis strictly linked to lipids and DNA oxidative damage [7].

Recently, altered impedance of blood cells have been suggested as a promising marker to diagnose ME/CFS [14,18]. Many studies have proved that peripheral blood mononuclear cells (PBMCs) of CFS/ME patients express biological stresses in the form of increased ATP metabolism [18,20,21], which leads to an increase in normalized impedance. However, little is known about the changes of the electrical characteristics of living muscle cells, which ME/CFS directly impacts. Inspired by the work with PBMSs by Esfandyarpour et al., our aim is to demonstrate the correlation between OS and impedance of single muscle cells. Although PBMCs are easier to obtain in a clinical setting, they are known to be oxidatively responsive to many diseases besides ME/CFS, including multiple sclerosis (MS), rheumatoid arthritis (RA), metabolic syndrome and diabetes [22–25].The manifestation of the oxidative stress levels in muscle cells would represent a more specific marker associated with ME/CFS. For this reason, we optimized a protocol which induces oxidative stress to mimic muscle oxidation in ME/CFS patients. The electrical properties of treated and untreated cells were characterized using broadband impedance spectroscopy in a microfluidic device.

There are many established benefits to diagnostics using electrical methods compared to the conventional biochemical or optical techniques due to lower requirements on time, resources, and trained personnel. Beyond the well-known Coulter counters for blood cell enumeration, microfluidics combined with electrical sensors have been demonstrated for evaluating various cellular properties in a lab-on-a-chip format [26]. Examples include determining efficacy of cardiac targeting therapies [27], monitoring oxygen and glucose consumption by cancer cells [28], detecting extracellular vesicle secretion [29], and measuring cell conduction and permeability [30]. Broadband impedance spectroscopy in the GHz frequency range previously demonstrated the ability to investigate intracellular impedance noninvasively, which has been applied to distinguish cell sizes, viability as well as properties of the cytoplasm and nucleus [31].

While electrical impedance spectroscopy has been applied in many studies to monitor toxicity in cell cultures [32–34], only a few researchers have implemented electrical sensors to characterize oxidative stress. For example, Deka et al. monitored the natural levels of hydrogen peroxide released from L6 muscle cells using cyclic voltammetry and electrochemical impedance spectroscopy [35]. In this context H_2O_2 has been extensively used to induce OS and it plays an active role in developing cytotoxicity, lipid peroxidation and oxidative DNA damage [36–39]. Furthermore, most of the electrical biosensors for the application of oxidative stress rely on cultured adherent cells, which requires more time for culture growth than running single cell detection on suspended cells in a microfluidic system. The adherent systems also inherently measure the cell attachment and depend on the contact surface area, as well as the cell migration to different electrode areas, making it difficult to reliably determine any intracellular properties. A recent method proved effective at identifying ME/CFS cells from healthy muscle cells using an adherent electrode platform and several metrics of impedance to extract cellular characteristics [14]. This nanosensor array focuses on measurements at 15 kHz, most efficient for sensing membrane capacitance and cell-surface interactions but leaving potential intracellular characteristics unstudied. To enable measurements of single cell oxidation, we use dielectrophoresis (DEP) to attract and disperse individual cells to and from the detection zone in a microfluidic channel. In addition, by implementing broadband electrical sensing in a microfluidic device, our system has the ability to reveal electrical characteristics of different cell compartments, as well as cell morphology [31]. With this setup, we aim to establish a cellular model that is responsive to oxidative imbalance, in which external H_2O_2 provokes intracellular mitochondrial disruption responsible for $O_2^{\cdot-}$ production and ion fluxes that could then be the focus of broadband impedance measurements.

2. Materials and methods

2.1. Cell culture

The L6 cells belong to an immortalized rat skeletal myoblast cell line (Cat.No. N.92102117, Sigma-Aldrich). The cells were cultured following the protocols from ATCC.

2.2. Oxidation protocol

Adherent cells were treated with regular culture medium supplemented with H_2O_2 at 5, 10 and 20 μM for 4, 6, 10 and 16 h. After the removal of the medium, cell viability was determined through Trypan blue (Sigma-Aldrich T8154) staining and optical characterization. Ten random frames of pictures were taken in each experimental condition. The built-up of oxidative products inside cells was determined by the nitroblue tetrazolium chloride (NBT, Sigma-Aldrich N6639) assay, in which NBT is reduced by $O_2^{\cdot-}$ into formazan and the resulting color change is detected spectrophotometrically by absorbance at 550 nm (Microplate 257 spectrometer; SPECTRAmax 190, Molecular Devices) [36].

2.3. Calcium imaging assay

Suspended cells were plated in 96-well plates with a concentration of 3000 cells per well. After incubation at 37 °C for 45 min the cells were loaded with Fura-2 AM (Life Technologies Molecular Probes #F1221) by adding a solution of NES (Normal External Solution Buffer, 140 mM NaCl, 2.8 mM KCl, 2 mM $CaCl_2$, 2 mM MgCl and 10 mM HEPES, pH7.4) supplemented with 10 mg/ml of Bovine Serum Albumin (Sigma-Aldrich #A9647) and 5μM Fura-2 AM. After incubation for 45 min at 37 °C at dark, the supernatant was removed. The cells were rinsed with NES for 15 min at room temperature and imaged afterwards. The cell imaging protocol has been described by Pietrangelo et al. [37] Briefly, the stained cells were sequentially and repetitively excited at 340 nm and 380 nm using a monochromator (Till Photonics, T.I.L.L Photonics, Germany) equipped with a 150W Xenon lamp. The fluorescence images were collected using a 40x oil objective lens connected to an intensified CCD camera (Hamamatsu Photonics, Hamamatsu Japan). The basal calcium state was acquired for 5 min before separate cells were treated using 5 μM Ionomycin (Sigma-Aldrich #13909) and 10 mM of EGTA (Sigma-Aldrich #E3889) in order to perform calibration of the fluorescence intensity corresponding to known calcium concentrations.

2.4. Microdevice design and assembly

The broadband electrical sensor has been reported previously, which contains three electrodes 200 μm wide, the side two being the ground electrodes while the central one tapering into a series gap (Fig. 1b) of 10 μm separation; this is a coplanar waveguide (CPW) design. The sensor has been used previously to inspect cytoplasmic impedance [31] and distinguish cell viability [40]. In this work the electrical sensor was coupled with a sheath focusing polydimethylsiloxane (PDMS) microfluidic channel to measure oxidative stress in muscle cells. The microchannel was treated using oxygen plasma, aligned by hand, and bonded to the electrical chip. Since only the PDMS channel was treated by oxygen plasma, but not the electrical chip, the two were bonded non-permanently. This allowed the electrical chip to be cleaned and reused. The channel has a cross section with a width of 200 μm and height of 100 μm, and was operated at a sample flow rate of 0.1 μL/min and a sheath flow rate of 0.25 μL/min. The device assembly was mounted on a Nikon fluorescence microscope (Nikon Eclipse Ti) so the cells under measurement could be observed in real time.

2.5. Electrical measurements

H_2O_2 treated or control L6 cells were suspended in an 8.5% sucrose solution at a concentration of 1×10^6 cells/mL as the sample solution. The same 8.5% sucrose solution without any cells was used as the sheath fluid. A vector network analyzer (VNA) was used to apply a trapping signal of −9 dBm at a frequency of 500 MHz. After single cells were trapped by dielectrophoresis (DEP), the trapping signal was switched to the sensing signal with a power of −15 dBm and the signal was swept from 9 kHz to 9 GHz. The reflection coefficient (S11) and transmission coefficient (S21) through the series gap were measured by the VNA. Each measurement was taken with the cell bridging the series gap followed with a subsequent measurement without the cell to determine the background signal of the cell-free solution. The same electrical chip was used for all the cell measurements, while our prior work found that chip-to-chip variability was low compared to the cell measurement sensitivity.

2.6. Data analysis

A python code was developed using the electrical signals of each cell and correlated background to find the difference at each frequency, which is the net contribution by the cells and referred to as either the ΔS11 or ΔS21. These signals were correlated with the cell size, displacement from the center of the electrodes as well as cell treatment through Nikon microscope images and optical characterization. The average ΔS11 and ΔS21 were fit using Advanced Design Systems through an electrical circuit model to extract dielectric parameters as described in previous works [41].

2.7. Optical characterization

The cell size was determined through images taken by the microscope at the end of the electrical measurement and analyzed using the FIJI/ImageJ software. The edges of the cells were traced manually, and the resulting area was used to calculate an estimate of the cell diameter. In addition, a line to the center of the electrodes was superimposed on every image to determine the displacement of the center of the cell from the center of the series gap. A separate characterization was done using a Coulter counter (Beckman) to ensure that the manually estimated cell size matched the overall population sizes of treated and untreated cells.

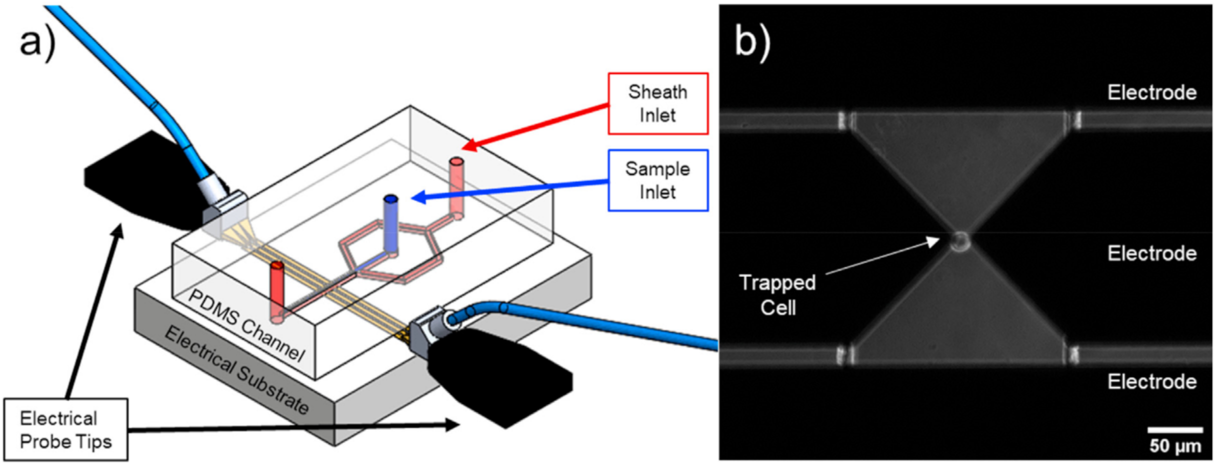

Fig. 1. a) A schematic showing the microfluidic setup to direct cells to the series gap in the power electrode. b) An image showing one cell captured by dielectrophoretic (DEP) and trapped in the series gap.

2.8. *Statistical analysis*

The data are reported as means ± standard deviation (SD). Differences between cellular populations were determined using analysis of variance (ANOVA). The cell density and NBT measurements were grouped by the treatment concentration and time. Later, the electrical measurements, ΔS11 and ΔS21, were compared at select gigahertz frequencies and plotted against the optically obtained measurements of size and displacement (55 control vs. 68 treated cells). Significance was indicated as $*p \leq 0.05$ and $**p \leq 0.01$ using a two-tailed Student's *t*-test. The calcium imaging data (234 control vs. 333 treated cells) were analyzed using the Mann-Whitney *U* test based on convention.

3. Results

3.1. *Cellular oxidation*

To introduce oxidative stress to L6 skeletal muscle cells, the cells were exposed to different concentrations of H_2O_2 for 4, 6, 10 and 16 h. The goal is to identify the combination of treatment time and concentration that has little impact on cell viability while allows build-up of oxidative stress over an extended period of time to mimic the chronic oxidative state. This goal aligns with the choice of H_2O_2 because it is a less aggressive free radical option that is still physiologically present. Fig. 2a shows the fraction of living cells as a function of the different treatment conditions. The living cell fraction was determined by dividing the number of living cells (not stained by Trypan blue) by the total cell number in each image. It is observed that the cell viability in every treatment group is lower than the control regardless of treatment time or concentration. Cells treated with different H_2O_2 concentrations of 5, 10 and 20 μM demonstrate comparable viability at 4 and 6 h. However, a H_2O_2 dose effect on the cell viability is observed at 10 h, where treatment with 20 μM H_2O_2 leads to a significant reduction of cell viability compared to treatment doses of 5 and 10 μM H_2O_2. As seen from Fig. 2a, the cell viability drops from 100% to 93 ± 4.5% and 87 ± 7.7% for cells exposed to 5 and 10 μM H_2O_2 respectively for 10 h to 76 ± 9.5% when the H_2O_2 concentration is elevated to 20 μM.

Furthermore, cell viability recovers at 16 h due to cell proliferation (Fig. 2a). To reduce the compounding effect from cell doubling, L6 cells were subsequently treated with H_2O_2 for 10 h at different concentrations of 0, 5, 10 and 20 μM. The NBT assay was used to characterize $O_2^{\cdot -}$ production, which is an indicator of the oxidative stress. The optical absorbance from the NBT assay is proportional to the concentration of $O_2^{\cdot -}$ inside cells. As shown in Fig. 2b, the absorbance values obtained from the samples are 0.40 ± 0.16 for the control, and 0.38 ± 0.10, 0.53 ± 0.20 and 0.59 ± 0.21 for cells treated with 5, 10 and 20 μM of H_2O_2 respectively. The absorbance values of the samples treated by 10 and 20 μM H_2O_2 are significantly higher than that of the control ($p < 0.05$), indicating more oxidative stress under these concentrations. Considering that 20 μM H_2O_2 has a significantly greater impact on the cell viability, L6 cells treated with 10 μM H_2O_2 for 10 h were used for further measurements described below. Physiologically, 10 μM H2O2 is a biologically relevant concentration at an intracellular level and it has been proven to correlate with oxidative stress which is a key characteristic of ME/CFS [7,22,42,43].

As the electrical measurements require a low conductive environment, we further tested if suspending cells in an isotonic sucrose solution would introduce changes in the oxidative stress compared to suspending cells in the physiological PBS solution. As shown in Fig. S1, neither the control nor the H_2O_2 treated cells suspended for 3 h in the two solutions demonstrate a significant difference in the $O_2^{\cdot -}$ concentration. Previous work has also shown that cell viability remains stable through 10 h in the sucrose solution [44]. These suggest that suspending cells in the sucrose solution does not interfere with the measurements of oxidative stress.

3.2. *Intracellular Ca^{2+}Imaging*

To quantify the intracellular Ca^{2+} concentration, both oxidized and control L6 cells were stained by a calcium sensitive dye, Fura-2 AM. The cells were then analyzed by fluorescence microscopy and the images were analyzed to determine the intracellular Ca^{2+} concentration of single cells. The oxidized L6 cells have an intracellular Ca^{2+} concentration of 65.6 ± 17.7 nM compared to 60.3 ± 11.9 nM for the control, and the difference is statistically significant ($p = 0.002$), with a small effect size of 0.156 and a statistical power of 92%. Comparing the histograms of the intracellular Ca^{2+} concentration from the two cell populations and the fit based on skewed normal distributions (Fig. 3), it is observed that the

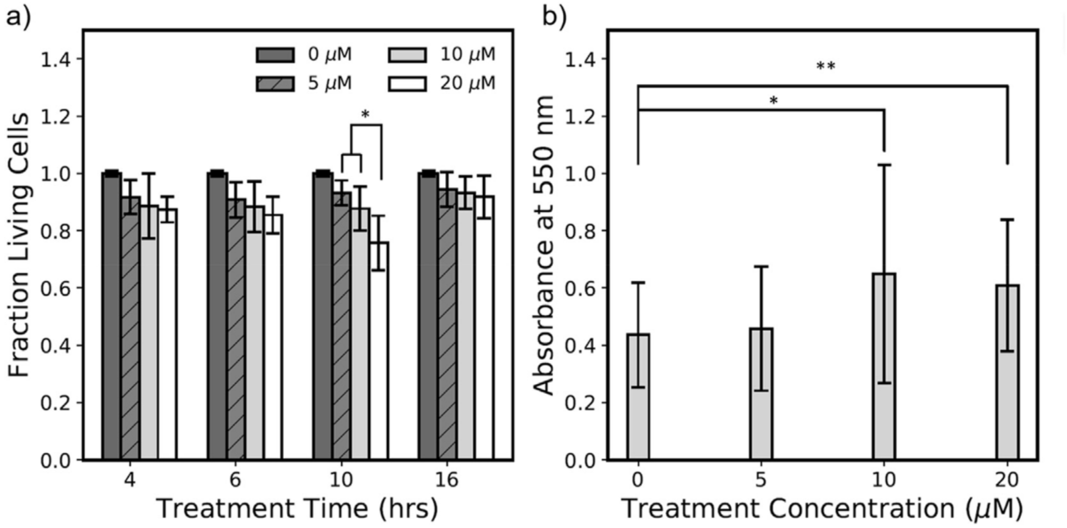

Fig. 2. a) Relative cell density after treatment by 0, 5, 10 and 20 μM H_2O_2 for 4, 6, 10 and 16 h. The cell densities were normalized by the values of the control cells inspected at the same time point. b) Absorbance at 550 nm of cells stained with NBT after treatment with 0, 5, 10 and 20 μM H_2O_2 for 10 h (* indicates $p < 0.05$, ** indicates $p < 0.01$.)

means are comparable at 47.38 and 45.47 nM, and the skew parameter on this data increases from 2.28 for control cells to 2.77 for treated cells. Thus, L6 oxidation leads to an increase of the intracellular Ca^{2+} concentration on average. In addition, intracellular Ca^{2+} concentration from the oxidatively stressed cells demonstrates a distinctly wider distribution.

3.3. Impedance change with oxidation state

Electrically, the ratios of power reflected (S11) and transmitted (S21) with single cells occupying the series gap were determined over broadband frequencies of 9 kHz to 9 GHz for a total of 55 untreated and 68 treated cells. To account for any background shift over time, each cell measurement was subtracted by a background measurement done immediately afterwards to get the ΔS11 and ΔS21 (Fig. S2). As the differences are most obvious in the MHz to GHz range, typical spectra of ΔS11 and ΔS21 of H_2O_2 treated cells and control cells are presented in Fig. 4a and b from 32 MHz–9 GHz. The ΔS11 for the control L6 cell shows a relatively flat line, which suggests that the impedance of the untreated cells resembles that of the cell-free solution. The treated cells mostly yield similar flat spectra of ΔS11 at the base line until the high MHz to GHz frequency range: the signals sometimes remain flat as the control cells, but in other cases have a pronounced dip (Response 1) or a pronounced peak (Response 2). For example, the two spectra corresponding to two oxidized cells with different responses have a peak and dip of 0.096 and −0.026 dB at 5.85 GHz. Such unique patterns suggest that the cells have different impedance profiles based on the response to oxidation. Similarly, the ΔS21 spectra of the control cells are mostly flat in the high MHz to GHz range, while the treated cells sometimes demonstrate peaks (Response 1) or dips (Response 2) in the ΔS21 spectra. In the sample spectra shown in Fig. 4b, the peak and dip at 7.54 GHz for the responses are 0.171 and −0.439 dB respectively. These peaks or dips show a distinct difference between the cells and the background signals from the sucrose solution, indicating that the treated cells have an obvious deviation in the power reading from the cell free solution compared to the control cells. The ΔS11 and ΔS21 signals in the kHz to low MHz range frequency are either lacking features or too noisy to be useful for cell detection (Fig. S2).

3.4. Model fitting to estimate dielectric parameters

We further used Keysight Advanced Design System (ADS) simulation to fit the ΔS11 and ΔS21 spectra and extract the impedance parameters of the cells. As the signal differences between treatment and control groups are most obvious in 100 MHz–9 GHz, we aimed for the best fit of the experimental data in this frequency range. The ΔS11 and ΔS21 from cells of each type was averaged for the fitting. A single shell model with membrane characteristics of 1 MOhm of resistance and 1 pF of capacitance was used to represent the cell membrane in the sucrose solution between two electrodes as described in our previous work on mammalian cell types [41]. With the frequency of 100 MHz–9 GHz, impedance contribution from the cell membrane becomes negligible, and the cytoplasm impedance R_c and C_c dominates. This means that the impedance difference between the treated and control cells results from change in the capacitance or resistance of the cytoplasm instead of the cell membrane [41]. The extracted R_c and C_c parameters are used to generate dielectric properties of the cytoplasm using equations (1) and (2) and a cell radius (r_o) of 8.25 μm.

$$\varepsilon_C = \frac{2C_c}{3\pi r_o} \tag{1}$$

$$\sigma_C = \frac{2}{\pi r_o R_c} \tag{2}$$

The resulting average dielectric parameters of each type of cells are summarized in Table 1.

Circuit analysis suggests that both types of stress responses could be caused by the increase of cytoplasmic conductivity and permittivity in the treated cells compared to the control cells. As the increase of Ca^{2+} concentration (Fig. 3) elevates the cytoplasmic conductivity, spectra in Fig. 4 could be contributed in part by the rise of the intracellular Ca^{2+} concentration. The opposite spectrum

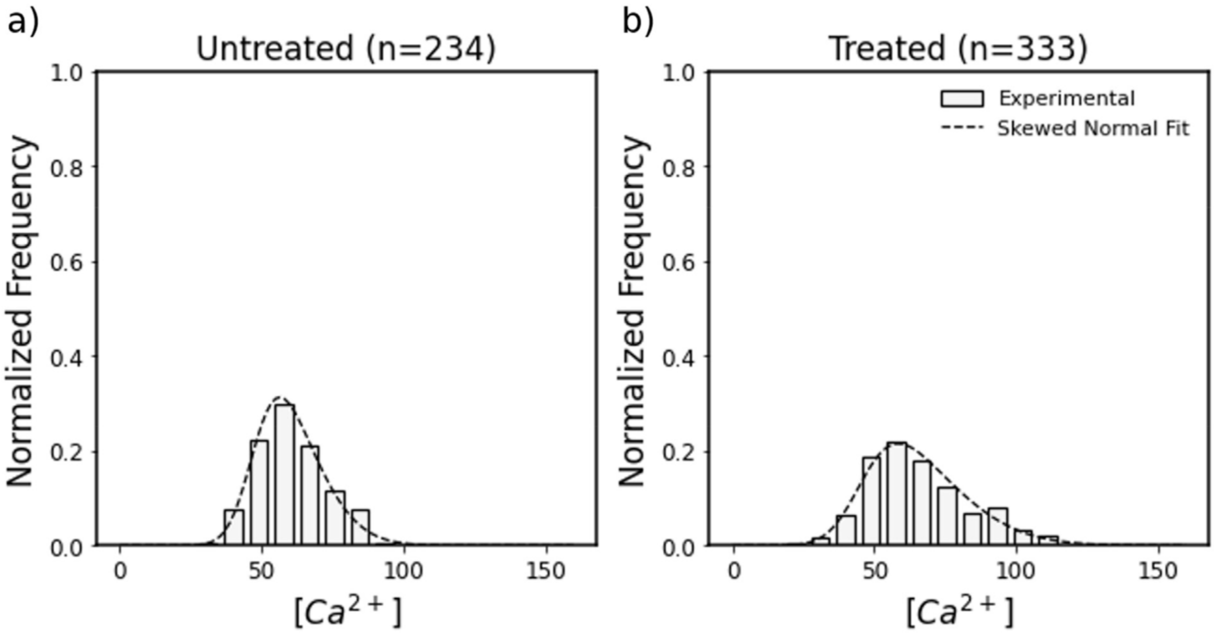

Fig. 3. Histograms of calcium concentration in (a) untreated cells and (b) cells treated with 10 μM H_2O_2 for 10 h.

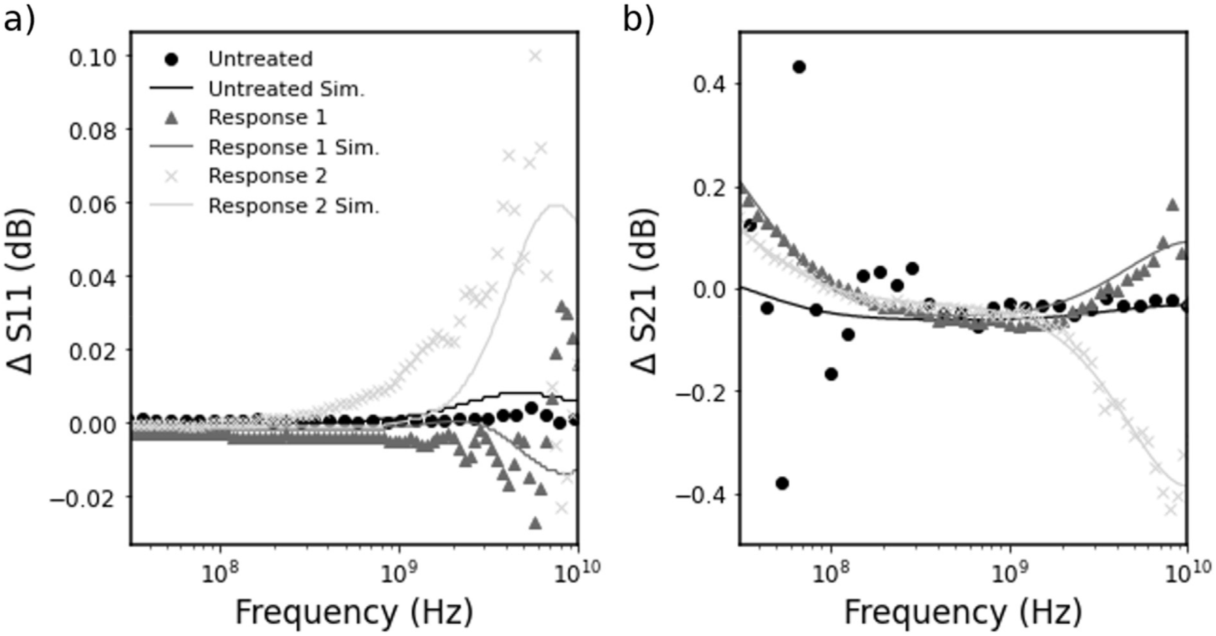

Fig. 4. Typical spectra of the ΔS11 (a) and ΔS21 (b) for control and treated cells. The symbols are from experimental measurements and lines are from simulation. The black symbols and lines are from control cells while the grey symbols and lines are from treated cells.

bending in the two types of stress response could be explained by electrical length difference of the tapered part of the transmission line inside the microfluidic channel. In the case of response 2 (peaks in ΔS11 and dips in ΔS21 spectra in the GHz range), there is a longer electrical length of the tapered CPW possibly attributed by more ion leakage from the cells, generating a higher signal than the control in ΔS11 and lower in ΔS21. The opposite of which is true for response 1. As the cells are continuously flowed into the device in a sucrose solution, the ionic microenvironment around individual cells reflects instantaneous ion flux from the cell. Thus, the microenvironment around each cell, theorized as the electrical length of the tapered CPW, is part of the cell electrical signature and contributes to their detection.

3.5. Electrical signal spread analysis at 7.5 GHz

The most apparent signal difference happens in both ΔS11 and ΔS21 at 7.54 GHz, as shown in Fig. 4. Therefore, the signal magnitude was compared for each captured cell against the optically measured size of the cell and distance from the center of the two electrodes, to determine the contribution of these variables. Fig. 5 shows ΔS11 of H_2O_2 treated and control cells vs. the optically measured variables. In this figure, it is clear that the untreated cells show a steady baseline around zero, while the treated cells show more obvious scattering properties. Similar differences are also observed in ΔS21 of H_2O_2 treated and control cells (Fig. S3). Among the cells captured, the control cell diameter ranged from 12.9 μm to 26.7 μm (16.66 ± 2.32 μm), meanwhile the treated cell diameter ranged from 11.5 μm to 22.1 μm (15.79 ± 2.06 μm). Ideally, the cell capture position would be consistent and right in the center of the two electrodes, however in both cases we verified that the maximum displacement was less than one cell diameter. The displacement for control cells was 5.39 ± 4.99 μm while for treated cells, it was 4.47 ± 4.00 μm. Based on the spread in Fig. 5 and Fig. S3, there is neither significant size change after the oxidation treatment nor significant difference in the cell position relative to the electrode center. Furthermore, the size and distance from electrode center do not have a correlation with any cells being recorded, for either ΔS11 or ΔS21. This ruled out the effect of cell size or any small variation in cell position in causing the unique spectra being observed. Additionally, ΔS11 or ΔS21 from cells are at least an order of magnitude greater than from the cell free solution. Thus, the difference in the electrical signals is caused by the impedance changes of the cytoplasm resulting from oxidative stress.

Table 1
Summary of the cytoplasmic conductivity (σ_c) and relative dielectric permittivity constant (ε_c) from simulation fitting the average spectra of each type, assuming membrane resistance is 1MOhm and 1 pF as an outer shell.

	σ_c (S/m)	ε_c (ε_o)
Untreated	0.22	9.49
Stress Response 1	0.35	11.22
Stress Response 2	0.28	12.94

Due to the greater visual distinction on the ΔS11 signal noted on both Figs. 4 and 5, we further fit histograms of ΔS11 signal spread at 7.54 GHz using a skewed normal model. Examining the fits in Fig. 6 (dashed lines), there is a slight shift of the mean in ΔS11 at 7.54 GHz from 0.0041 to −0.017 dB in populations of cells that have been treated. The shift in ΔS11 is consistent with the increase of Ca^{2+} concentration previously discussed in Fig. 3, potentially linking the electrical changes in oxidized cells with intracellular ion management in the cytoplasm and mitochondria. More noticeably, the distribution among ΔS11 flattens. Similar flatting is also observed of the ΔS21 distribution after cell oxidation (Fig. S4). These are consistent with wider distribution of the intracellular Ca^{2+} concentration that were reported in Section 3.3. The distribution of S-parameters thus suggests that elevated intracellular Ca^{2+} concentration associated with the oxidative stress could be measured using the broadband electrical sensor, thereby reducing the time and resources required for disease monitoring. The impedance sensor thus holds a great potential for monitoring oxidative stress in single cells for diagnostic purposes.

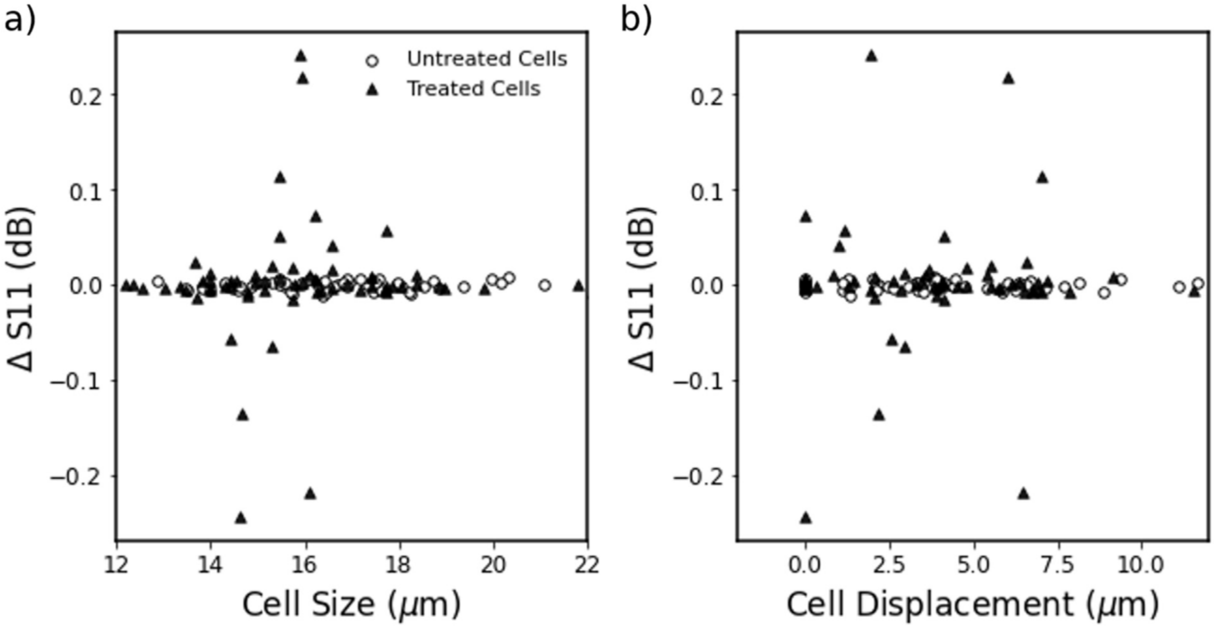

Fig. 5. Scatterplot representing ΔS11 comparison with cell diameter (a) and displacement (b) at 7.54 GHz.

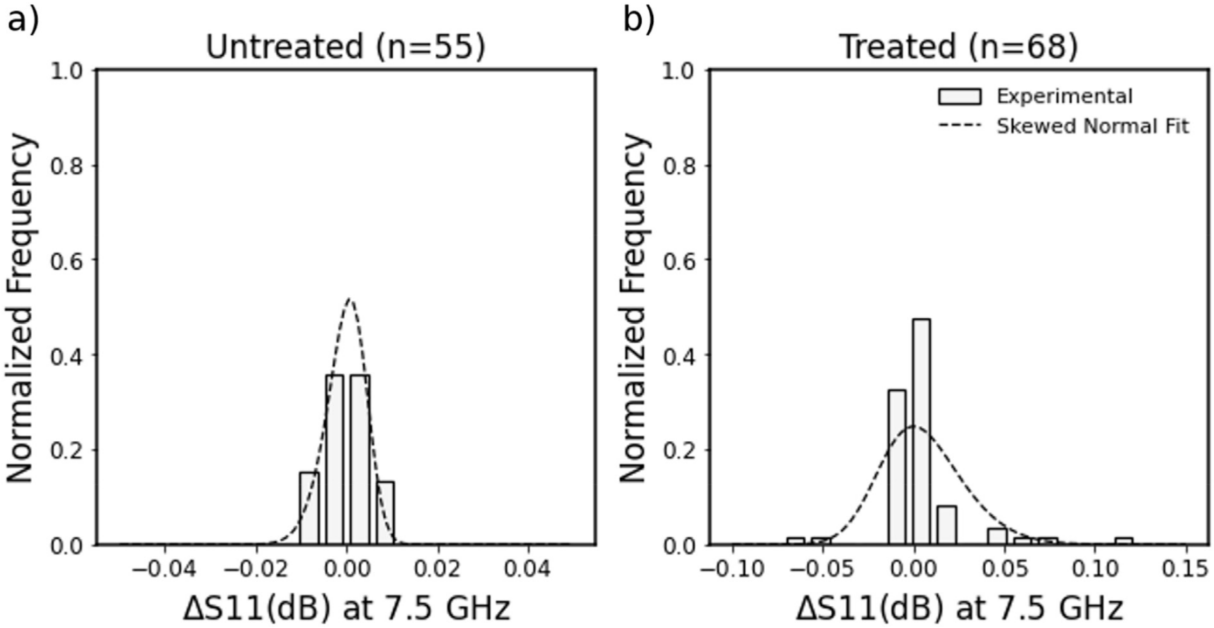

Fig. 6. Histogram showing distribution of electrical signal ΔS11 among (a) untreated cells and (b) cells treated with $10 \mu M H_2O_2$for 10 h.

4. Discussion

As described above, distinct differences have been measured electrically between skeletal muscle cells subjected to H_2O_2 treatments versus the untreated controls. While the control cells are electrically homogeneous with relatively flat ΔS11 and ΔS21 signals in the 100 MHz−9 GHz range, the oxidatively stressed cells separate into those that resemble the control and those that deviate from the control. In the frequency range of 100 MHz to 9 GHz inspected here, the impedance difference results from change in the capacitance or resistance of the cytoplasm or organelles, rather than of the external membrane [41]. It was also previously established that cell size and apoptosis can change the signal in single Jurkat cells in sucrose, so these were ruled out by image analysis and comparison, as shown in Fig. 5 [30,40]. Instead, circuit analysis suggests that the cells electrically different from the control experiences increase of cytoplasmic conductivity and permittivity. The conductivity increase indicates a buildup of ions within the cells, consistent with the release of calcium from the endoplasmic reticulum into the cytoplasm to cope with the oxidative stress. The calcium concentration also varies as cells adapt to the oxidative stress, leading to recovery of the cytoplasmic resistance. This results in only a small fraction of oxidized cells having intracellular Ca^{2+} concentration above the rest state threshold (Fig. 3) or having S parameters deviating from the control cells (Fig. 4). Although the exact mechanism requires further investigation, we can speculate that in our oxidative stress model, exogenous H_2O_2 entering the cells triggers the increase of the $O_2^{\cdot-}$ through mitochondrial electron leakage and alteration of the mitochondrial membrane potential.

The wide variation of the spectra from treated cells are likely due to the multiple mechanisms and stages by which reactive oxygen species change the properties of the cytoplasm: 1) the buildup of calcium ions in the cytoplasm, 2) reduction of lysosomes and 3) subsequent destruction of the cell membrane [45,46]. When lysosomes are disrupted, iron concentration in the cytoplasm increases from nano-molar to micro-molar and the calcium concentration can elevate from the nano-molar range to the milli-molar range in extreme cases of ion release [47,48]. These ion concentration changes by orders of magnitude could explain the significant and unique signal differences between H_2O_2 treated cells and the control. In a previous study, the secretion of H_2O_2 from healthy L6 cells was found to cause an increase of conductivity between the cell and electrode using electrochemical impedance spectroscopy [35]. The conductivity change in this study was seen both with and without removal of calcium, indicating multiple pathways of cell oxidation. Previous analysis of H_2O_2 concentration on cells has also shown electrically distinct changes in cell membrane potential due to iron changes in treated cells, which was separate from the calcium dependent pathway [49]. In our study, the distributions of intracellular calcium concentration in treated vs. control cells match those of the S parameters between the two groups of cells, supporting the correlation between calcium flux and altered electrical properties.

A big factor in the response spread may be due to the individuality of the cells and the ability of oxidative stress to damage different organelles. As discussed above, the oxidative stress is a multi-step process, and each cell will undergo those steps with a different timing. Hydrogen peroxide, upon entering the cell leads to subcellular component damage in different organelles through superoxide production and changes the electrical properties in different areas. Moreover, the cells adapt themselves and scavenge the superoxide anion production either through stimulated mechanisms as in our case or endogenously as during physiopathological processes. For each cell measured, the cell could experience different points of the cascade process. As individual cells travel along the channel, the measurements reflect a temporary state of the individual cells rather than a permanently acquired oxidative damage.

While cells with ME/CFS do not produce $O_2^{\cdot-}$ by direct conversion of exogenous H_2O_2, the cellular pathways related to mediating $O_2^{\cdot-}$ could be similar to those we observed during H_2O_2 treatment. The organelles involved are important Ca^{2+} reservoirs that absorb and stabilize intracellular Ca^{2+} when its level increases in the cytosolic compartment [50]. The key to oxidative stress management at a cellular level seems to be in the moderation of calcium and other intracellular ions through several mechanisms that become active based on the chronic stress state. These mechanisms related to the distribution of ions and protein charges across the mitochondrial membrane appear similarly in ME/CFS cells and notably show both upregulation and downregulation when oxidation occurs [20]. These cytoplasmic ion fluxes and the subsequent destruction of intracellular membranes contribute to cytoplasmic conductivity and permittivity changes, resulting in the observed alteration of the electrical characteristics of the oxidatively stressed cells.

Seeing these changes is useful for not only diagnostic tools, but also increasing basic understanding of muscular disease progression at a cellular level. Especially for ME/CFS, the diagnosis is often based on symptoms, leading to work in electronic biomarker recognition to identify affected blood cells [14]. However, our device has the capability to look at muscle samples without culturing cells directly onto a device, making it reusable and applicable to real time monitoring of the cell oxidative stress. We recognize that the electrical sensing approach may not offer the specificity of molecular and biochemical methods, while the holistic view of single cells may represent the pathology more comprehensively, especially considering single biomarkers have failed to diagnose ME/CSF. The utilization of electrical sensing coupled with companion biological characterization may also offer insights about the source of electrical alternation. Currently, the time limiting steps in our measurements are manually triggering the instruments for cell injection and trapping, and the measurement throughput is on the order of minutes per cell. With automation and streamlining of controls, we expect a significant improvement of the throughput for measuring clinical samples. A real-time, sensitive, microfluidic set-up makes it a potential option to monitor disease progression and test potential treatment efficacy by providing relevant information about the disease state of muscle.

5. Conclusion

In this study, we saw a direct correlation between the generation of reactive oxygen species in living cells through treatment with 10 μM of H_2O_2 for 10 h and a deviation from the electrical characteristics of untreated cells. The change due to oxidative state was seen in both the reflected and transmitted signals in a way that was independent of the cell position between the electrodes or their size. We have shown that a single shell model can adequately simulate the dielectric properties of the cell cytoplasm to differentiate those under oxidative stress from the normal ones. Comparable distributions of the intracellular calcium concentration and S parameters suggest the correlation of these two variables. Based on these findings, it would be possible to identify some cells experiencing a stress response and future work will determine how the sign and magnitude of a signal changes based on specific intracellular property changes associated with reactive oxygen species as $O_2^{\cdot-}$. This tool could be used in many pathologies to perform an early diagnosis, using the different patterns obtained with the electrical device and offers a promising reusable technique for screening. Beyond diagnosis, there is an opportunity to learn more about how cellular stress works and how diseases like ME/CFS and other muscular disorders progress.

CRediT authorship contribution statement

Caroline Ferguson: Conceptualization, Methodology, Software, Validation, Formal analysis, Investigation, Data curation, Writing – original draft, Visualization. **Niccolo Pini:** Conceptualization, Methodology, Validation, Formal analysis, Investigation, Data curation, Writing – original draft, Visualization. **Xiaotian Du:** Software, Validation, Formal analysis, Writing – review & editing. **Marco Farina:** Writing – review & editing. **James M.C. Hwang:** Writing – review & editing. **Tiziana Pietrangelo:** Conceptualization, Data curation, Writing – review & editing, Supervision, Project administration, Funding acquisition. **Xuanhong Cheng:** Conceptualization, Resources, Data curation, Writing – review & editing, Supervision, Project administration, Funding acquisition.

Declaration of competing interest

The authors declare that they have no known competing financial interests or personal relationships that could have appeared to influence the work reported in this paper.

Acknowledgements

We greatly appreciate the funding sources that made this work possible. CF, XD and XC are supported through funding from National Science Foundation-ECCS 1809623. CF also appreciates the support of the Koerner Family Foundation. NP has a PhD fellowship (code n. DOT1353500) in the framework of PON RI 2014/2020, Action I.1—"Innovative PhDs with industrial characterization", funded by Ministry of Education, University and Research (MIUR), Italy, FSE-FESR, which was instrumental in establishing this international collaboration. TP was supported by 'G. d'Annunzio' University grants.

Appendix A. Supplementary data

Supplementary data to this article can be found online at https://doi.org/10.1016/j.aca.2021.338678.

References

[1] R. Brigelius-Flohé, Commentary: oxidative stress reconsidered, Genes Nutr. 4 (2009) 161–163, https://doi.org/10.1007/s12263-009-0131-8.

[2] A. Dasgupta, K. Klein, Chapter 2 - methods for measuring oxidative stress in the laboratory, in: A. Dasgupta, K. Klein (Eds.), Antioxidants in Food, Vitamins and Supplements, Elsevier, San Diego, 2014, pp. 19–40, https://doi.org/10.1016/B978-0-12-405872-9.00002-1.

[3] M. Valko, D. Leibfritz, J. Moncol, M.T.D. Cronin, M. Mazur, J. Telser, Free radicals and antioxidants in normal physiological functions and human disease, Int. J. Biochem. Cell Biol. 39 (2007) 44–84, https://doi.org/10.1016/j.biocel.2006.07.001.

[4] D. Harman, Aging: a theory based on free radical and radiation chemistry, J. Gerontol. 11 (1956) 298–300, https://doi.org/10.1093/geronj/11.3.298.

[5] M. Marrone, R.M.L. La Rovere, S. Guarnieri, E.S. Di Filippo, G. Monaco, T. Pietrangelo, G. Bultynck, S. Fulle, R. Mancinelli, Superoxide anion production and bioenergetic profile in young and elderly human primary myoblasts, 2018, Oxid. Med. Cell. Longev. (2018), https://doi.org/10.1155/2018/2615372, 2615372.

[6] S. Fulle, P. Mecocci, G. Fanó, I. Vecchiet, A. Vecchini, D. Racciotti, A. Cherubini, E. Pizzigallo, L. Vecchiet, U. Senin, M.F. Beal, Specific oxidative alterations in vastus lateralis muscle of patients with the diagnosis of chronic fatigue syndrome, Free Radic. Biol. Med. 29 (2000) 1252–1259, https://doi.org/10.1016/S0891-5849(00)00419-6.

[7] T. Pietrangelo, S. Fulle, F. Coscia, P.V. Gigliotti, G. Fanò-Illic, Old muscle in young body: an aphorism describing the Chronic Fatigue Syndrome, Eur. J. Transl. Myol. 28 (2018), https://doi.org/10.4081/ejtm.2018.7688.

[8] T. Pietrangelo, R. Mancinelli, L. Toniolo, G. Montanari, J. Vecchiet, G. Fanò, S. Fulle, Transcription profile Analysis of vastus lateralis muscle from patients with chronic fatigue syndrome, Int. J. Immunopathol. Pharmacol. 22 (2009) 795–807, https://doi.org/10.1177/039463200902200326.

[9] K.G. Brurberg, M.S. Fønhus, L. Larun, S. Flottorp, K. Malterud, Case definitions for chronic fatigue syndrome/myalgic encephalomyelitis (CFS/ME): a systematic review, BMJ Open 4 (2014), e003973, https://doi.org/10.1136/bmjopen-2013-003973.

[10] B.M. Carruthers, Definitions and aetiology of myalgic encephalomyelitis: how the Canadian consensus clinical definition of myalgic encephalomyelitis works, J. Clin. Pathol. 60 (2007) 117, https://doi.org/10.1136/jcp.2006.042754.

[11] A.L. Komaroff, L. Bateman, Will COVID-19 lead to myalgic encephalomyelitis/chronic fatigue syndrome? Front. Med. 7 (2021) https://doi.org/10.3389/fmed.2020.606824.

[12] J. Castro-Marrero, M. Faro, L. Aliste, N. Sáez-Francàs, N. Calvo, A. Martínez-Martínez, T.F. de Sevilla, J. Alegre, Comorbidity in chronic fatigue syndrome/myalgic encephalomyelitis: a nationwide population-based cohort study, Psychosomatics 58 (2017) 533–543, https://doi.org/10.1016/j.psym.2017.04.010.

[13] L.D. Devanur, J.R. Kerr, Chronic fatigue syndrome, J. Clin. Virol. 37 (2006) 139–150, https://doi.org/10.1016/j.jcv.2006.08.013.

[14] R. Esfandyarpour, A. Kashi, M. Nemat-Gorgani, J. Wilhelmy, R.W. Davis, A nanoelectronics-blood-based diagnostic biomarker for myalgic encephalomyelitis/chronic fatigue syndrome (ME/CFS), Proc. Natl. Acad. Sci. U.S.A. 116 (2019) 10250, https://doi.org/10.1073/pnas.1901274116.

[15] L. Lorusso, S.V. Mikhaylova, E. Capelli, D. Ferrari, G.K. Ngonga, G. Ricevuti, Immunological aspects of chronic fatigue syndrome, Autoimmun. Rev. 8 (2009) 287–291, https://doi.org/10.1016/j.autrev.2008.08.003.

[16] K.J. Moneghetti, M. Skhiri, K. Contrepois, Y. Kobayashi, H. Maecker, M. Davis, M. Snyder, F. Haddad, J.G. Montoya, Value of circulating cytokine profiling during submaximal exercise testing in myalgic encephalomyelitis/chronic fatigue syndrome, Sci. Rep. 8 (2018) 2779, https://doi.org/10.1038/s41598-018-20941-w.

[17] J.G. Montoya, T.H. Holmes, J.N. Anderson, H.T. Maecker, Y. Rosenberg-Hasson, I.J. Valencia, L. Chu, J.W. Younger, C.M. Tato, M.M. Davis, Cytokine signature associated with disease severity in chronic fatigue syndrome patients, Proc. Natl. Acad. Sci. U.S.A. 114 (2017) E7150, https://doi.org/10.1073/pnas.1710519114.

[18] R.K. Naviaux, J.C. Naviaux, K. Li, A.T. Bright, W.A. Alaynick, L. Wang, A. Baxter, N. Nathan, W. Anderson, E. Gordon, Metabolic features of chronic fatigue syndrome, Proc. Natl. Acad. Sci. U.S.A. 113 (2016) E5472, https://doi.org/10.1073/pnas.1607571113.

[19] J.B. Prins, J.W. van der Meer, G. Bleijenberg, Chronic fatigue syndrome, Lancet 367 (2006) 346–355, https://doi.org/10.1016/S0140-6736(06)68073-2.

[20] J.C. Booth, N.D. Orloff, J. Mateu, M. Janezic, M. Rinehart, J.A. Beall, Quantitative permittivity measurements of nanoliter liquid volumes in microfluidic channels to 40 GHz, IEEE Trans. Instrum. Meas. 59 (2010) 3279–3288, https://doi.org/10.1109/TIM.2010.2047141.

[21] M. Gerwyn, M. Maes, Mechanisms explaining muscle fatigue and muscle pain in patients with myalgic encephalomyelitis/chronic fatigue syndrome (ME/CFS): a review of recent findings, Curr. Rheumatol. Rep. 19 (2017) 1, https://doi.org/10.1007/s11926-017-0628-x.

[22] G. Galita, O. Brzezińska, I. Gulbas, J. Sarnik, M. Poplawska, J. Makowska, T. Poplawski, Increased sensitivity of PBMCs isolated from patients with rheumatoid arthritis to DNA damaging agents is connected with inefficient DNA repair, JCM 9 (2020) 988, https://doi.org/10.3390/jcm9040988.

[23] C. Pistono, M.C. Monti, C. Boiocchi, F.G. Berzolari, C. Osera, G. Mallucci, M. Cuccia, A. Pascale, C. Montomoli, R. Bergamaschi, Response to oxidative stress of peripheral blood mononuclear cells from multiple sclerosis patients and healthy controls, Cell Stress Chaperones 25 (2020) 81–91, https://doi.org/10.1007/s12192-019-01049-0.

[24] M. Monserrat-Mesquida, M. Quetglas-Llabrés, X. Capó, C. Bouzas, D. Mateos, A. Pons, J.A. Tur, A. Sureda, Metabolic syndrome is associated with oxidative stress and proinflammatory state, Antioxidants 9 (2020) 236, https://doi.org/10.3390/antiox9030236.

[25] S. Belia, F. Santilli, S. Beccafico, L.D. Feudis, C. Morabito, G. Davì, G. Fanò, P.M.A. Mariggiò, Oxidative-induced membrane damage in diabetes lymphocytes: effects on intracellular Ca2 + homeostasis, Free Radic. Res. 43 (2009) 138–148, https://doi.org/10.1080/10715760802629588.

[26] K. Hiramoto, K. Ino, Y. Nashimoto, K. Ito, H. Shiku, Electric and electrochemical microfluidic devices for cell analysis, Front. Chem. 7 (2019) 396, https://doi.org/10.3389/fchem.2019.00396.

[27] B.M. Maoz, A. Herland, O.Y.F. Henry, W.D. Leineweber, M. Yadid, J. Doyle, R. Mannix, V.J. Kujala, E.A. FitzGerald, K.K. Parker, D.E. Ingber, Organs-on-Chips with combined multi-electrode array and transepithelial electrical resistance measurement capabilities, Lab Chip 17 (2017) 2294–2302, https://doi.org/10.1039/C7LC00412E.

[28] P.M. Misun, J. Rothe, Y.R.F. Schmid, A. Hierlemann, O. Frey, Multi-analyte biosensor interface for real-time monitoring of 3D microtissue spheroids in hanging-drop networks, Microsyst Nanoeng 2 (2016) 16022, https://doi.org/10.1038/micronano.2016.22.

[29] T. Akagi, K. Kato, M. Kobayashi, N. Kosaka, T. Ochiya, T. Ichiki, On-chip immunoelectrophoresis of extracellular vesicles released from human breast cancer cells, PloS One 10 (2015), e0123603, https://doi.org/10.1371/journal.pone.0123603.

[30] X. Ma, X. Du, C.R. Multari, Y. Ning, C. Palego, X. Luo, V. Gholizadeh, X. Cheng, J.C.M. Hwang, Broadband single-cell detection with a coplanar series gap, in: 2015 86th ARFTG Microwave Measurement Conference, IEEE, Atlanta, GA, USA, 2015, pp. 1–3, https://doi.org/10.1109/ARFTG.2015.7381459.

[31] X. Du, C. Ladegard, X. Ma, X. Cheng, J.C.M. Hwang, Ultra-wideband electrical sensing of nucleus size in a live cell, in: 2019 49th European Microwave Conference (EuMC), IEEE, Paris, France, 2019, pp. 208–211, https://doi.org/10.23919/EuMC.2019.8910779.

[32] J.M. Seiffert, M.-O. Baradez, V. Nischwitz, T. Lekishvili, H. Goenaga-Infante, D. Marshall, Dynamic monitoring of metal oxide nanoparticle toxicity by label free impedance sensing, Chem. Res. Toxicol. 25 (2012) 140–152, https://doi.org/10.1021/tx200355m.

[33] T. Sun, H. Morgan, Single-cell microfluidic impedance cytometry: a review, Microfluid. Nanofluidics 8 (2010) 423–443, https://doi.org/10.1007/s10404-010-0580-9.

[34] Y. Yuste, J.A. Serrano, A. Olmo, A. Maldonado-Jacobi, P. Pérez, G. Huertas, S. Pereira, F. de la Portilla, A. Yúfera, Monitoring muscle stem cell cultures with impedance spectroscopy, in: Proceedings of the 11th International Joint Conference on Biomedical Engineering Systems and Technologies, SCITEPRESS - Science and Technology Publications, Funchal, Madeira, Portugal, 2018, pp. 96–99, https://doi.org/10.5220/0006712300960099.

[35] K. Deka, J. Kumar, A. Bhowmick, S. Banu, D.K. Das, Silver nanoparticle modified Pt electrode as voltammetric and electrochemical impedance sensor for hydrogen peroxide in live biological cells, Indian J. Chem. (2018) 5.

[36] S. Burattini, P. Ferri, M. Battistelli, A. D'emilio, L. Biagiotti, P. Sestili, M.B.L. Rocchi, E. Falcieri, Apoptotic DNA fragmentation can be revealed in situ: an ultrastructural approach, Microsc. Res. Tech. 72 (2009) 913–923, https://doi.org/10.1002/jemt.20735.

[37] D. Caporossi, S.A. Ciafrè, M. Pittaluga, I. Savini, M.G. Farace, Cellular responses to H2O2 and bleomycin-induced oxidative stress in L6C5 rat myoblasts, Free Radic. Biol. Med. 35 (2003) 1355–1364, https://doi.org/10.1016/j.freeradbiomed.2003.08.008.

[38] H. Nohl, A.V. Kozlov, L. Gille, K. Staniek, Cell respiration and formation of reactive oxygen species: facts and artefacts, Biochem. Soc. Trans. 31 (2003)

1308–1311, https://doi.org/10.1042/bst0311308.
[39] B. Yang, T.N. Oo, V. Rizzo, B. Yang, T.N. Oo, V. Rizzo, Lipid rafts mediate H2O2 prosurvival effects in cultured endothelial cells, Faseb. J. 20 (2006) 1501–1503, https://doi.org/10.1096/fj.05-5359fje.
[40] H. Li, C. Multari, C. Palego, X. Ma, X. Du, Y. Ning, J. Buceta, J.C.M. Hwang, X. Cheng, Differentiation of live and heat-killed E. coli by microwave impedance spectroscopy, Sensor. Actuator. B Chem. 255 (2018) 1614–1622, https://doi.org/10.1016/j.snb.2017.08.179.
[41] X. Ma, X. Du, C.R. Multari, Y. Ning, X. Luo, V. Gholizadeh, C. Palego, X. Cheng, J.C.M. Hwang, Reproducible broadband measurement for cytoplasm capacitance of a biological cell, in: 2016 IEEE MTT-S International Microwave Symposium (IMS), IEEE, San Francisco, CA, 2016, pp. 1–4, https://doi.org/10.1109/MWSYM.2016.7540262.
[42] H. Sies, Role of metabolic H2O2 generation: redox signaling and oxidative stress, J. Biol. Chem. 289 (2014) 8735–8741, https://doi.org/10.1074/jbc.R113.544635.
[43] K.B. Norheim, G. Jonsson, R. Omdal, Biological mechanisms of chronic fatigue, Rheumatology 50 (2011) 1009–1018, https://doi.org/10.1093/rheumatology/keq454.
[44] C. Palego, C. Merla, Y. Ning, C.R. Multari, X. Cheng, D.G. Molinero, G. Ding, X. Luo, J.C.M. Hwang, Broadband microchamber for electrical detection of live and dead biological cells, in: IEEE MTT-S International Microwave Symposium Digest, (MTT), 2013, 2013, pp. 1–3, https://doi.org/10.1109/MWSYM.2013.6697355.
[45] G. Ermak, K.J.A. Davies, Calcium and oxidative stress: from cell signaling to cell death, Mol. Immunol. 38 (2002) 713–721, https://doi.org/10.1016/S0161-5890(01)00108-0.
[46] Q. Hu, S. Corda, J.L. Zweier, M.C. Capogrossi, R.C. Ziegelstein, Hydrogen peroxide induces intracellular calcium oscillations in human aortic endothelial cells, Circulation 97 (1998) 268–275, https://doi.org/10.1161/01.CIR.97.3.268.
[47] (n.d.) Tashi G. Kinjo, P.M. Paul, Schnetkamp, Ca2+ chemistry, storage and transport in biologic systems: an overview, https://www.ncbi.nlm.nih.gov/books/NBK5959/?report=printable. (Accessed 10 February 2020).
[48] H. Xu, D. Ren, Lysosomal physiology, Annu. Rev. Physiol. 77 (2015) 57–80, https://doi.org/10.1146/annurev-physiol-021014-071649.
[49] L. Firek, A. Beresewicz, Hydrogen peroxide induced changes in membrane potentials in Guinea pig ventricular muscle: permissive role of iron, Cardiovasc. Res. 24 (1990) 493–499, https://doi.org/10.1093/cvr/24.6.493.
[50] T. Pietrangelo, E.S. Di Filippo, R. Mancinelli, C. Doria, A. Rotini, G. Fanò-Illic, S. Fulle, Low intensity exercise training improves skeletal muscle regeneration potential, Front. Physiol. 6 (2015), https://doi.org/10.3389/fphys.2015.00399.